Microstructure and Properties of the LDEDed Cu-Bearing Martensitic Stainless Steel After a Single-Step Tempering Treatment

Hongmei Zhu[1] · Li Zhao[1] · Baichun Li[1] · Longzhang Shen[1] · Changjun Qiu[1]

Abstract

431 martensitic stainless steels (MSS) alloying with copper (Cu, 0–3.5 wt%) have been fabricated by a laser directed energy deposition technology and treated by a single-step tempering treatment. The microstructure and properties of the tempered MSS specimens have been carefully investigated by various advanced techniques, including XRD, SEM, EBSD, TEM, microhardness tester, universal material testing machine, and electrochemical workstation. The results show that the Cu-free 431 MSS is mainly composed of lath-shaped martensite, a few patches of austenite and carbide, while the martensite matrix is refined with the increased austenite and nano-precipitates by increasing Cu content of the Cu-bearing MSS. Consequently, the microhardness of the Cu-bearing 431 MSS specimens increases firstly and then decreases, reaching the maximum value (472 $HV_{0.2}$) at the Cu level of 2.5 wt%. In comparison to the Cu-free 431 MSS, the addition of 2.5 wt% Cu could lead to a striking comprehensive performance, including tensile properties with ultimate tensile strength (UTS) of 1576 MPa, yield strength (YS) of 1258 MPa and elongation (EL) of 16.1%, as well as improved corrosion resistance by an order of magnitude. The mechanisms behind the variation in the overall performance of the Cu-bearing 431 MSS specimens were discussed in detail.

Keywords Laser directed energy deposition · Martensitic stainless steel · Cu alloying · Microstructure · Properties

1 Introduction

AISI 431 martensitic stainless steel (MSS) has been widely used in marine engineering and aviation fields due to its inherent merits such as excellent mechanical properties and moderate corrosion resistance [1, 2]. However, it is the poor weldability and the required two-step heat treatment (including quenching at 950–1050 °C and tempering at 275–350 °C) that have restricted the engineering applications of 431 MSS [1].

Laser directed energy deposition (LDED) provides an opportunity for directly near net manufacturing of large components with complete dense and high performance [4–9], which has been applied extensively in manufacturing and remanufacturing high-performance MSS, such as AISI 410 [4] AISI 420 [5, 6] and 18Ni300 [7, 8]. Howbeit, there are only a few studies to report the influences of processing parameters [2, 9–11], post-heat treatment [1, 12, 13], and Mo alloying elements [14] on laser fabrication of 431 MSS. For instance, Liu et al. [1] discovered that the microstructural homogeneity and tensile properties of the LDEDed 431 MSS could be improved by optimizing the heat treatment parameters. The optimum tensile properties, with a strength of 1283 MPa and elongation (EL) of 14.5%, were obtained after a tempering treatment (680 °C × 2 h) + solution treatment (1050 °C × 45 min) + tempering treatment (315 °C × 3 h) [1]. In addition, Wang et al. [14] reported that the M/F ratio could be decreased by Mo alloying in 431 MSS, leading to a reduction of the microhardness with increasing Mo contents (0–6 wt%), but the wear resistance could be significantly improved by the microstructure refinement and the formation of M_2C hard phase. Besides, the corrosion resistance was increased first and then decreased, which could be optimized at the Mo content of 2 wt% [14].

It is widely accepted that the mechanical properties of cast MSS could be significantly enhanced by Cu alloying, due to a precipitation strengthening effect via a suitable heat treatment [15–20]. Ye et al. [18] investigated the effects of the Cu

✉ Hongmei Zhu
  meizihong999@126.com

✉ Changjun Qiu
  qiuchangjun106@126.com

1 Provincial Key Laboratory of Advanced Laser Manufacturing Technology, University of South China, Hengyang 421001, China

contents (0 wt%, 1.5 wt% and 3 wt%) on mechanical properties of cast 15%Cr super MSS after a 1050 °C×30 min solid solution and 600 °C×2 h tempering treatment. The results indicated that the 3 wt% Cu addition could result in 62% improvement in the product of strength and elongation (PSE) compared to the Cu-free MSS. Huang et al. [19] found that the Rockwell hardness of the 420 MSS could be increased by adding 4 wt% Cu, due to the undissolved carbides and Cu-rich precipitation after a 1040 °C×30 min solid-solution treatment. In addition, the corrosion resistance of the MSS can be remarkably affected by Cu alloying [20–22]. For example, Ma et al. [21] verified that a stable passivation film could be formed by adding 3 wt% Cu, and thus the corrosion resistance was greatly enhanced for the cast 0Cr13Ni4Mo MSS after a 1050 °C×2 h solid solution and 500 °C×2 h tempering treatment. Meanwhile, Zhang et al. [22] demonstrated that the corrosion resistance of cast Fe–Cr–W-based alloys in a sulfuric acid solution could be significantly improved by the addition of 2 wt% Cu.

Nevertheless, to the best of authors' knowledge, the Cu alloying in 431 MSS has scarcely been investigated to date. Hence, we aimed at developing MSS with excellent mechanical properties and improved corrosion resistance via Cu alloying. Due to the relatively low mechanical properties of the as-deposited specimens (see "Appendix"), a single-step tempering treatment at 600 °C for 1 h was adopted in this work, and the microstructure and properties of the tempered 431 MSS with various Cu contents (0–3.5, in wt%) have been carefully examined. This study will be of great significance for achieving high performance and short-process preparation of the Cu-bearing MSS, especially laser manufacturing and remanufacturing of complex-shaped steel components with ultra-high strength and ductility.

2 Experimental

Gas-atomized 431 MSS powders containing different Cu contents, with an average particle size of 75 μm, were used as feed stock for LDED in this work. The substrate was A36 steel with a dimension of 110 mm×60 mm×15 mm (length, width, thickness). The chemical composition of 431 MSS powders was 0.11 C, 16.53 Cr, 2.69 Ni, 0.94 Si, 0.87 Mn, and balance Fe (in wt%). Five different 431 MSS specimens containing 0% Cu, 1% Cu, 1.5% Cu, 2.5% Cu and 3.5% Cu were fabricated by the LDED method, referring as 0Cu, 1Cu, 1.5Cu, 2.5Cu and 3.5Cu, respectively. To achieve a uniform distribution, the powders were mixed using the QM-3SP04L ball mill at a speed of 120 r/min for 2 h, and the mixed powders were then dried in a furnace at 100 °C for 2 h prior to the laser deposition process.

The MSS specimens was deposited using a FL-1500 1.5 kW fiber laser with a coaxial powder-feeding and water-cooling system, as sketched in Fig. 1a. The laser processing parameters are as followings: laser power density of 430 W/mm², laser scanning speed of 480 mm/min, overlapping rate of 50% and powder delivery rate of 6.5 g/min. High-purity N_2 (99.999%) was used as both a shielding gas and a carrier gas with a flow rate of 10 L/min. The as-deposited specimens, with the size of 90 mm×40 mm×4 mm, was tempered at 600 °C for 1 h and finally cooled in air.

To achieve a flat surface, the topmost about 1 mm in thickness of the tempered MSS specimens was machined off using a grinding machine (Fig. 1b). Tensile samples were all machined with their loading axes parallel to the laser scanning direction, with the geometry as shown in
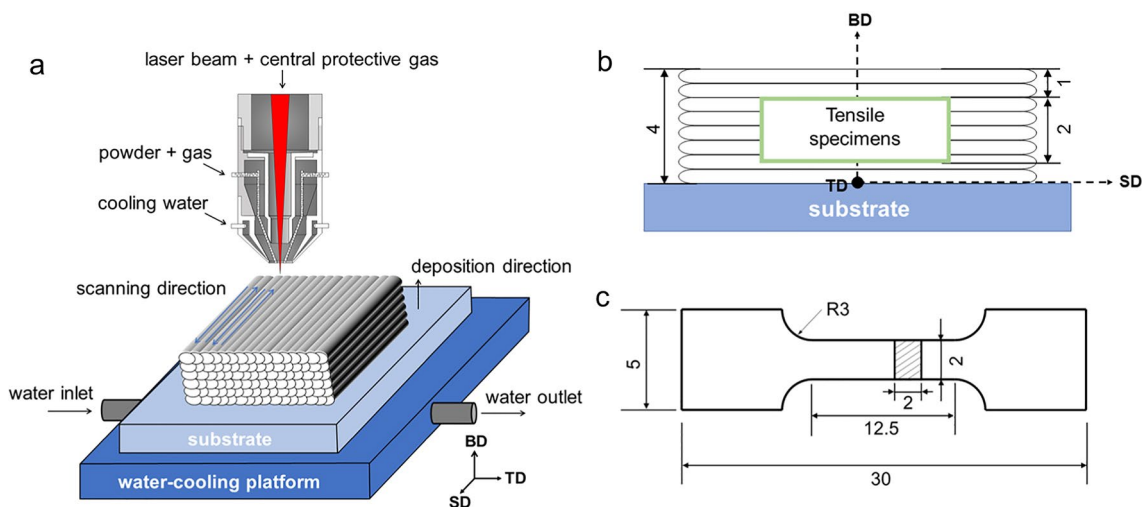

Fig. 1 **a** LDED process; **b** Schematic of the sectioned tensile specimen position from the sample; **c** Geometry of the tensile specimen in mm scale. TD, SD and BD represents transverse direction, scanning direction and building direction, respectively

Fig. 1c. The tensile test was performed using a PWS-E100 universal testing machine at a constant displacement rate of 0.2 mm/min. Two tensile specimens were selected for each to ensure the repeatability and reliability of the results. In addition, the microhardness was determined using a MHV-2T microhardness tester with a load of 200 g and a dwell time of 10 s. The reported hardness values are the average of at least five separate measurements. The corrosion resistance was tested using a CS300 electrochemical workstations during immersion in a 3.5% NaCl solution at room temperature. The potentiodynamic polarization curves were obtained with a potential range from − 1.5 V to 1.0 V at a scan rate of 10 mV/s, with the saturated calomel electrode as the reference electrode and a platinum electrode as the counter electrode, respectively.

The metallographic specimens were mechanically ground and polished prior to etching in aqua regia for about 3 s. The phase constituents of the samples were carefully examined using a Miniflex600 X-ray diffractometer (XRD) with a Cr source. The acceleration voltage and current were 40 kV and 40 mA, respectively. The specimens were scanned in the 2θ range from 20° to 90° with a step size of 0.02°. The microstructure of the tempered specimen was investigated using a MERLIN scanning electron microscope (SEM) with energy dispersive spectrometer (EDS). The working distance and accelerating voltage were about 10 mm and 20 kV, respectively. The EBSD measurement was carried out using FEI Nova NanoSEM 450 coupled with an EDAX detector under an accelerating voltage of 20 kV. The AZtecCrystal software was used to reconstruct the prior austenite and measure the grain size. A detailed examination of the microstructural features were performed by a JEOL-2100 transmission electron microscope (TEM) operated at 200 kV. The TEM specimens were punched from ground thin foils, and then electropolished in a solution of 10% perchloric acid and 90% ethanol at a temperature of 25 °C.

3 Results and Discussion

3.1 Microhardness and Microstructure of the Tempered 431-*x*Cu MSS

3.1.1 Microhardness

Figure 2 shows the microhardness distribution and histogram of tempered 431 MSS specimens with different Cu contents (0–3.5 wt%). Noticeably, the negligible variation in the microhardness suggests a homogeneous microstructure in all the fabricated samples. Compared with the average microhardness of the tempered Cu-free MSS specimens (372 $HV_{0.2}$), the microhardness of the tempered Cu-bearing MSS specimens increases firstly and then decreases with increasing Cu content (Fig. 2b). The tempered 431–2.5Cu MSS specimen exhibits the highest microhardness of 472 $HV_{0.2}$, which is ~ 100 $HV_{0.2}$ higher than that of the tempered Cu-free MSS. Thus, it can be concluded that the microhardness of tempered 431 MSS could be enhanced by adding Cu element. In comparison to the tempered 431–2.5Cu MSS specimen, however, there is a slight reduction in microhardness of the tempered 431–3.5Cu MSS. The detailed reason will be analyzed by XRD and SEM hereinafter.

3.1.2 Phase Constituent

The XRD profiles of the tempered 431-*x*Cu MSS specimens (*x* = 0–3.5 wt%) are presented in Fig. 3. As seen from Fig. 3a, the tempered Cu-free 431 MSS specimen primarily
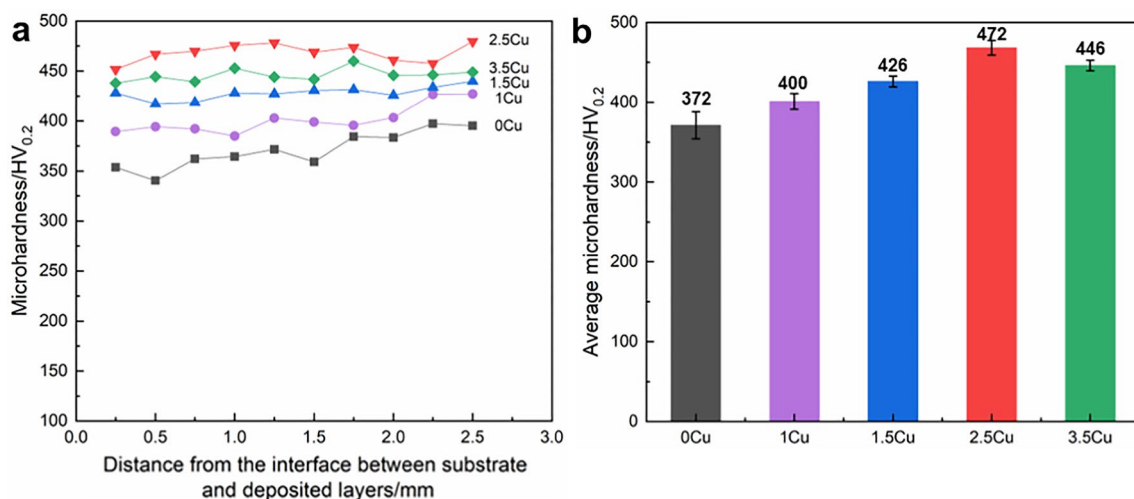

Fig. 2 The microhardness of the tempered 431-*x*Cu MSS: **a** Microhardness distribution; **b** Average microhardness histogram
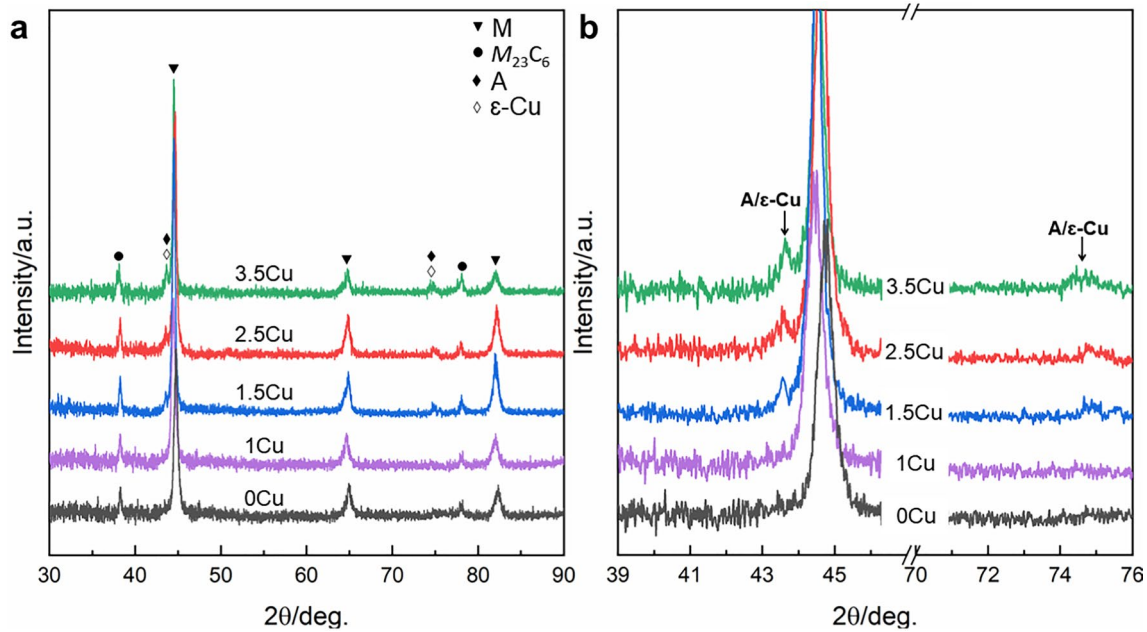
Fig. 3 XRD analysis of the tempered 431-*x*Cu MSS specimens: **a** XRD profiles; **b** Enlarged diffraction peaks in the 2θ range from 39° to 49° and 70° to 76°

consists of martensite (M) and carbide ($Cr_{23}C_6$), whereas the 1.5Cu, 2.5Cu and 3.5Cu MSS specimens exhibit additional diffraction peaks associated with the Cu-enriched phases (ε-Cu) and austenite (A). It is worth mentioning that the diffraction peaks of the ε-Cu and A are almost overlapped due to the similar lattice parameters [22]. However, there are no diffraction peaks of A in the 0Cu and 1.0Cu MSS samples, probably due to the low austenite content beyond the minimum detection limit of the XRD instrument.

Figure 3b compares the enlarged diffraction peaks of A and ε-Cu in the tempered 431-*x*Cu MSS specimens. Apparently, the intensity of A/ε-Cu peaks increases successively with the increasing Cu content. This can be attributed to the fact that the element Cu could promote the formation of A as well as the precipitation of ε-Cu during tempering [15, 16, 18, 23, 24].

In addition, the M peaks at 45° in the Cu-bearing MSS specimens obviously shift to the lower angle (44.4°), in comparison with that of the tempered 431 specimens. According to Brag diffraction law, the leftward shift of M peaks can be explained by the large lattice parameters and crystal plane spacing owing to the doping of Cu atoms (128 pm) with larger atomic radius than Fe (126 pm) [25]. This is similar to our previous work that the addition of V [26] or Nb [6] with a larger atomic radius than Fe atoms resulted in the leftward shift of the M diffraction peaks for the MSS. Additionally, the theoretical solubility of Cu in α-Fe is about 2.1 wt% at the eutectoid temperature of 835 °C, but decreases rapidly to 0.2 wt% at room temperature according to the

Fe–Cu phase diagram [18]. However, the Cu-enriched phase could not precipitate in time because of the non-equilibrium capture of the Cu atoms during rapid cooling LDED process (10^4–10^5 K/s), and thus the Cu-bearing supersaturated solid solution was obtained. This well explains the leftshift of M diffraction peak in the 431-1Cu specimens, without no further shift with the Cu content exceeding 1.5%.

3.1.3 SEM Morphology

Figure 4 presents SEM micrographs of the cross-section tempered 431-*x*Cu MSS samples. Apparently, the specimens were mainly composed of the lath-shaped martensite and gradually refined with increasing Cu content. It can be inferred that the Cu alloying could inhibit the grain growth, and thus lead to a significant refinement of the martensite lath in the tempered 431 MSS. This is in good agreement with the refinement effect of the Cu alloying in MSS reported by Gao et al. [15] and Ye et al. [18]. Furthermore, the white particles in Fig. 4e1 were analyzed by EDS, indicating a chemical composition of 8.13C, 17.96Cr, 2.74Ni, 1.53Si, 4.59Cu and balance Fe (in wt%). It can be deduced that the co-precipitation of $Cr_{23}C_6$ and ε-Cu occurred in the tempered Cu-bearing MSS, and increased with increasing Cu content.

Based on the aforementioned analysis, the reasons accounting for the remarkable microhardness improvement by the Cu addition are as followings: (1) Solid solution strengthening. The solid solution of Cu atom, demonstrated
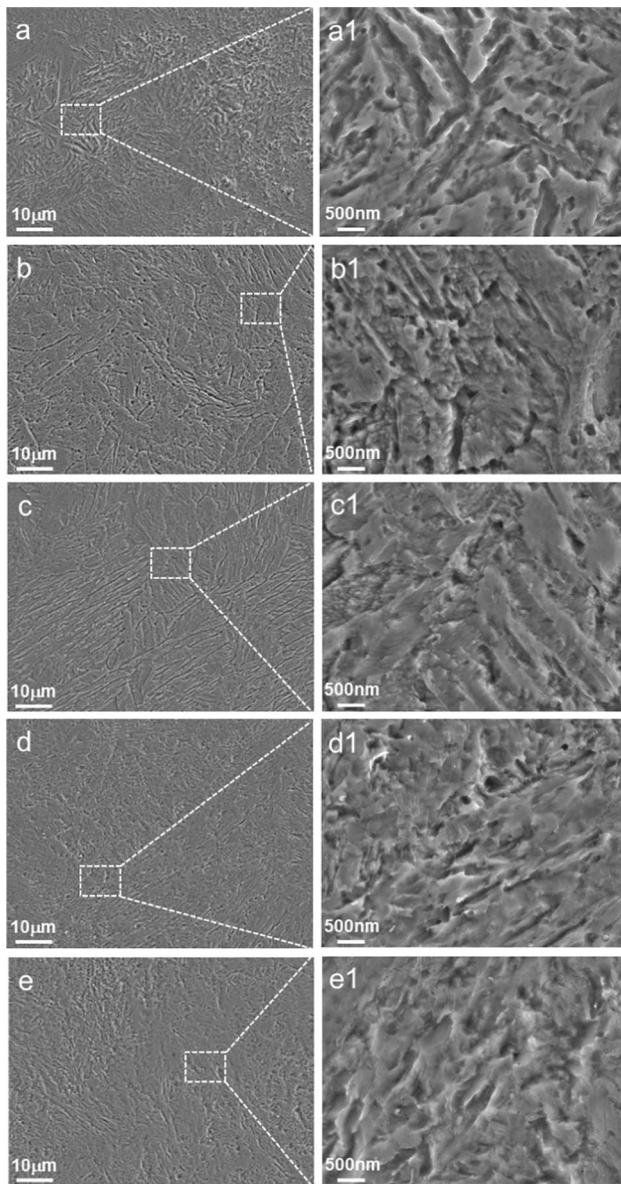
Fig. 4 SEM images of the tempered 431-*x*Cu MSS specimens: **a** 0Cu; **b** 1.0Cu; **c** 1.5Cu; **d** 2.5Cu; **e** 3.5Cu

by the XRD results (Fig. 3), could hinder the dislocation movement by generating the lattice distortion. (2) Grain refinement strengthening. The width of lath-shaped martensite was clearly reduced and thus enhance the microhardness according to the Hall–Petch relationship, caused by the solute-dragging effect of Cu atoms during the LDED process as well as the strong pinning effect of Cu on dislocation during tempering [27]. (3) Pecipitation strengthening. The Cu addition promoted the formation of ε-Cu precipitates (Fig. 4), and thus could block the dislocation movement according to the Ashby-Orowan mechanism [17, 28]. In addition, the reduced microhardness of the 431-3.5Cu can be explained by a larger volume fraction of austenite

together with a negligible variation of ε-Cu, as demonstrated by XRD in Fig. 3 and SEM in Fig. 4.

In view of the phase constituent and microhardness results, the tensile and corrosion properties of the tempered 431 MSS and 431-2.5Cu MSS were compared, and the detailed TEM characterization was conducted in order to explore the microstructural factors in the following section.

3.2 Tensile/Corrosion Properties and EBSD/ TEM Microstructure of the Tempered 431 and 431-2.5Cu MSS

3.2.1 Tensile Properties

Figure 5a and b present the tensile curves and properties of the tempered 431 MSS and 431-2.5 Cu MSS specimens. Clearly, the tempered 431 MSS specimen exhibits a UTS of 1197 MPa, a YS of 957 MPa and an EL of 13.7%. The 2.5 wt% Cu addition leads to a substantial improvement in both strength (UTS: 1576 MPa, YS: 1258 MPa) and ductility (EL: 16.1%). Based on the aforementioned analysis, the Cu alloying played a vital role in the refinement of the martensite lathes and the formation of nanoprecipitates such as ε-Cu phase.

Table 1 lists the tensile properties of the tempered 431 MSS and 431-2.5Cu MSS developed in this study, and is compared with those LDEDed and wrought 431 MSS samples from the literatures [1, 12]. Apparently, the 431-2.5Cu MSS exhibits a striking combination of high strength and high ductility after a single-step tempering of 600 °C × 1 h in this work.

Figure 5c and d displays the tensile fracture characteristics of the tempered 431 MSS and 431-2.5Cu MSS, respectively. The morphology of the fracture surface can be utilised to deduce the fracture mechanism of a material. The cracks originates from the center of the fracture, showing apparent necking deformation with fiber area and shear lip (inset of Fig. 5c, d). The fracture surface of the tempered 431 MSS exhibits a mixed fracture mode containing ductile fracture portions and quasi-cleavage fracture zones, featured by tearing ridges and quasi-cleavage planes as shown in Fig. 5c. Comparatively, the tempered 431-2.5Cu MSS exhibits typical ductile failure with the presence of massive equiaxed dimples, and a few small cleavage planes can be observed on the fracture surface (Fig. 5d).

As well-known, the diameter and depth of the dimple are closely related to the ductility of the material [29]. As determined in Fig. 5c and d by software Image-J, the dimple diameter of the tempered 431-2.5Cu and Cu-free 431 MSS specimens is 1.89 μm and 1.13 μm, respectively. Meanwhile, it can be observed from Fig. 5c and d that the dimple depth of the tempered 431-2.5Cu MSS sample is slightly larger than that of the tempered 431 MSS sample.
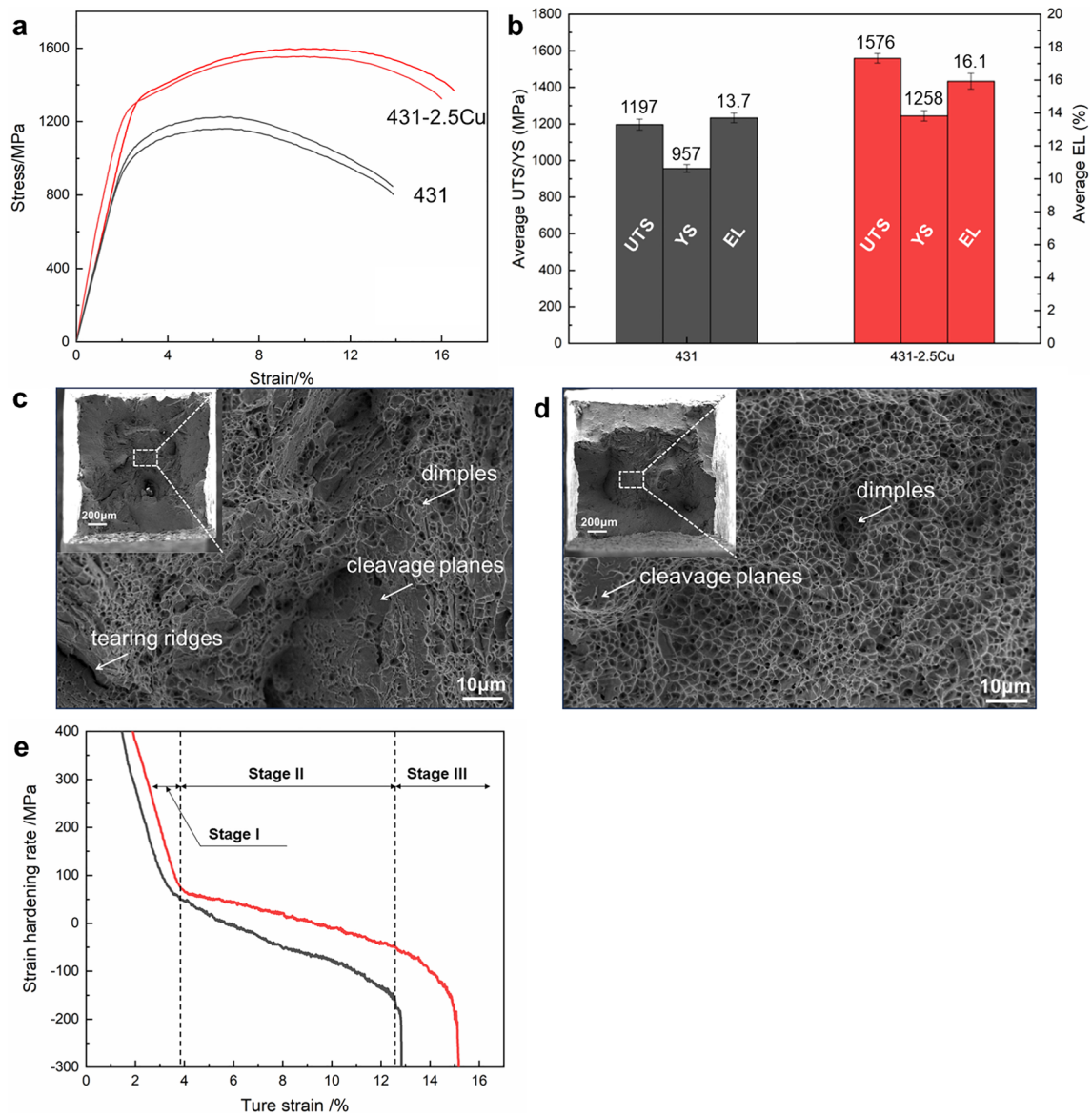
Fig. 5 Tensile curves **a**, histogram with average values **b**, fracture morphologies of the tempered 431 **c** and 431-2.5Cu **d** MSS specimens, strain hardening rate curves **e**

Table 1 Comparison of tensile properties of LDEDed and wrought 431 MSS

Methods	Specimens	UTS/MPa	YS/MPa	EL/%	Heat treatment	Reference
LDED	431 MSS	1197	957	13.7	Tempering (600 °C × 1 h)	This work
	431-2.5Cu	1576	1258	16.1		
LDED	431 MSS	905		16.3 ± 0.8	Tempering (680 °C × 2 h)	[1]
LDED	431 MSS	1283		14.5 ± 1.5	Tempering (680 °C × 2 h) + Solid solution (1050 °C × 45 min) + Tempering (315℃ × 3 h)	[1]
Wrought	431 MSS	1645	1080	13	Annealing (640 °C × 2 h) + Solid solution (1070 °C × 0.5 h) + Tempering (200 °C × 1 h)	[12]

Therefore, the larger diameter and depth of the dimples in the tempered 431-2.5Cu MSS could reasonably have a higher absorption energy during the plastic deformation process, resulting in an improvement in ductility.

Based on the above SEM and XRD results, the tempered 431 MSS is composed of coarse lath-shaped martensite and $Cr_{23}C_6$. The former martensite lathes could provide a large number of microcrack initiation sites and crack propagation paths, leading to the formation of a brittle fracture or microcracks [30]. Meanwhile, the latter dispersed $Cr_{23}C_6$ nano-particles could become promote the nucleation, growth and coalescence for microvoid, leading to ductile fracture [31]. Therefore, a mixed fracture was observed for the tempered 431 MSS (Fig. 5c).

In contrast, the ductility of the tempered 431-2.5Cu MSS was improved by the synergy effects of the refined lathed martensite, a higher volume fraction of A and the nano-sized ε-Cu precipitates. In addition, it is noted that the austenite, as a soft phase with favorable plasticity and toughness, can be responsible for the ductility improvement [32]. Specifically, the existence of ε-Cu precipitates could enhance the ductility by reducing the crack nucleation location and improving the crack propagation path [17, 33]. Therefore, a ductile fracture was observed for the tempered 431-2.5Cu MSS (Fig. 5d).

In order to further discuss the ductility improvement in the tempered 431-2.5Cu MSS, the strain hardening rate of the tempered 431 and 431-2.5Cu MSS were calculated, and the results are as presented in Fig. 5e. It is obvious that the strain hardening rate curves exhibits a three-stage characteristic. At stage I with low strain and stage III near fracture, the strain hardening rate undergoes a precipitous decrease, possibly due to its ineffectiveness in dislocation generation and accumulation during deformation [34]. In contrast, the strain hardening rate at stage II decreases gradually with the increasing strain. Noteworthily, the tempered 431-2.5Cu MSS (1.07) exhibits much lower strain hardening exponent (n) than the Cu-free tempered 431 MSS (3.92). As well-known, the lower strain hardening exponent is, the higher toughness of the material is. The enhanced strain hardening rate of the tempered 431-2.5Cu can be ascribed to the austenite-martensitic phase transformation during deformation, triggering the transformation-induced plasticity (TRIP) effect [35]. This has been verified in Niu's work [25], in which the larger the strain hardening rate could make the conditions for plastic instability to be met at higher strains. Therefore, the onset of necking was postponed to a larger deformation. Consequently, an increase in the uniform elongation and UTS was obtained in the tempered 431-2.5Cu MSS.
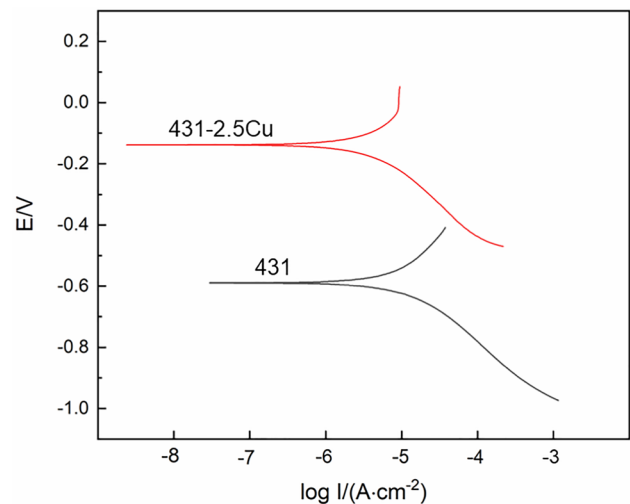

Fig. 6 Polarization curves of the tempered 431 and 431-2.5Cu MSS

Table 2 Electrochemical corrosion parameters of the tempered 431 and 431-2.5Cu MSS

Specimen	Electrochemical		
	Corrosion potential (SCE) E_{corr}/V	Corrosion current density I_{corr}/(A cm^{-2})	Corrosion rate / (mmpy)
431	−0.58651	1.5753×10^{-5}	0.15278
431-2.5Cu	−0.14173	2.0279×10^{-6}	0.01967

3.2.2 Corrosion Resistance

Figure 6 presents the potentiodynamic polarization curves of the tempered 431 MSS and 431-2.5Cu MSS in a 3.5 wt% NaCl solution. The corresponding electrochemical parameters are listed in Table 2. Obviously, the corrosion potential (E_{corr}) of the tempered 431-2.5Cu MSS (− 0.14173 V) is much higher than tempered 431 MSS (− 0.58651 V). This implies that the Cu addition could lower the corrosion tendency of the tempered 431 MSS. In comparison to the tempered 431 MSS, the corrosion current density (I_{corr}) and the corrosion rate of the tempered 431-2.5Cu MSS was significantly reduced approximately by an order of magnitude. Therefore, the 2.5 wt% Cu addition could remarkably enhance the corrosion resistance of the tempered 431MSS under the reported conditions.

The improved corrosion resistance of the tempered 431-2.5Cu MSS, relative to that of the tempered Cu-free 431 MSS, could be associated with the following aspects. (1) The increased austenite amount. As an element of austenite stabilizer, the introduction of Cu could dramatically facilitate the formation of austenite by promoting martensite → austenite phase transformation [15, 16, 18, 24, 25]. It is widely

accepted that austenite is beneficial to the passive film stability of the martensitic steels [32], and thus the corrosion resistance of the tempered 431-2.5Cu MSS with a larger volume fraction of austenite phase are superior to that of the tempered Cu-free 431 MSS. (2) The induced lattice distortion. Liu et al. [32] reported that the adhesion and stability of the passivation film could be greatly promoted, due to the increased surface energy induced by the lattice distortion. Herein, the XRD results in Fig. 3 reveal that the Cu addition led to the peak leftshift of the martensite phase. Accordingly, the corrosion resistance of the Cu-bearing MSS could be improved. (3) The promoted Cr enrichment. The element Cu could increase the Cr content in the oxide film of the Cu-bearing MSS surface, promoting the enrichment of Cr in the passivation film [26]. Consequently, the facilitated formation of Cr_2O_3 on the specimen surface could create a dense barrier that block the contact of sensitive ions (Cl^-) with the substrate, and thus improving the corrosion resistance of the tempered 431-2.5Cu MSS.

3.2.3 EBSD Characterization

Figure 7 features IPF maps of the martensite microstructure and reconstructed prior austenite. In comparison to the tempered 431 MSS (Fig. 7a), the martensitic lathes in the tempered 431-2.5Cu MSS are significantly refined (Fig. 7d), in good agreement with the SEM results. According to the Ref. [36], the single prior austenite grain can be divided into packets, blocks, sub-blocks and lathes by the orientation relationships. Generally, the prior austenite grains can be reconstructed from the

martensite orientation maps using the Kurdjumov–Sachs (K–S) orientation relationship (O.R.) [37]. Figure 7b and e show the reconstructed parent IPF map of the martensite microstructure, revealing a drastic discrepancy in the prior austenite grain size of two specimens. By calculating the equivalent circle diameter, the determined average grain size in the tempered 431-2.5Cu MSS (Fig. 7f) is greatly finer than that in the tempered 431 MSS (Fig. 7c). Therefore, it is reasonably concluded that the Cu addition could effectively refine the prior austenite and consequently the martensitic lathes.

The refinement of Cu alloying on the LDEDed 431 MSS can be ascribed to two main aspects. One is the extraordinary metallurgical environment, that is, the rapid cooling rate during the LDED process could effectively refine the grains [6]. The other is that the nucleation location of austenite could be occupied by the dissolved Cu atoms, exerting a strong solute-dragging effect on the migration of the austenite grain boundaries, and thus inhibiting the austenite growth [18, 38]. The preceding austenite refinement will undoubtedly lead to a decrease in the size of the martensite lathes [39]. The ε-Cu, precipitated along dislocations and grain boundaries, has a strong pinning effect on the grain boundary migration and prevents the grain growth of martensite lath in the tempering process [23, 28]. It is noted that the martensite lath of the 3.5Cu specimen is equivalent to the 2.5Cu specimen, which is probably due to the similar volume fraction of nanoprecipitates ε-Cu (Figs. 3, 4). This is similar to the results of Ye et al. [18], in which no further refinement of martensite lathes was observed when the Cu content was increased to 3 wt% in the cast 15% Cr super MSS.
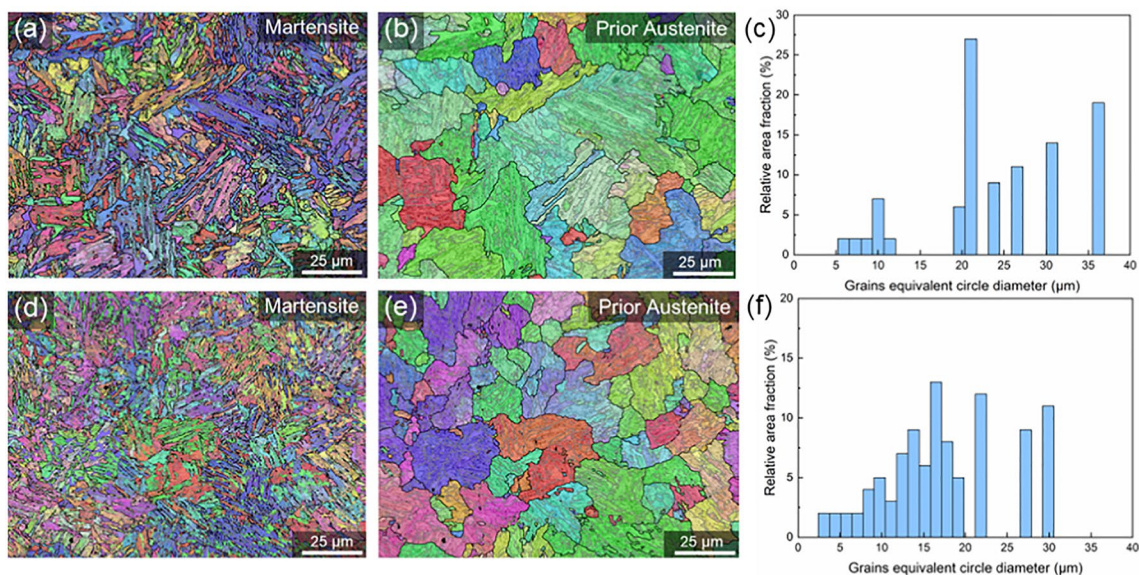

Fig. 7 EBSD results of the tempered 431 (**a–c**) and 431-2.5Cu (**d–f**) MSS specimens: **a**, **d** inverse pole figure (IPF) maps; **b**, **e** the reconstruction images of the prior austenite grain boundary; **c**, **f** the grain size distribution of prior austenite

3.2.4 TEM Measurement

In order to reveal the in-depth microstructural details, TEM characterization of the tempered 431 and 431-2.5Cu MSS specimens were carried out, as shown in Fig. 8. Apparently, the tempered 431 MSS specimen predominately consists of lath-shaped martensite matrix, over which carbide and a few patches of austenite are distributed (Fig. 8a, d). Comparatively, the tempered 431-2.5Cu MSS is composed of the refined martensite, over which austenite and nano-precipitates are observed with much larger volume fractions (Fig. 8e, h). Among them, the austenite nears the K–S O.R. with the martensite inside a prior austenite grain.

As shown in Fig. 8b and f, austenite (A) exists in the appearance of dark needles or bulks among the lath martensite. Given the high cooling rates during the LDED process together with the presence of the austenite forming element Ni, an incomplete martensitic transformation could be promoted and consequently the occurrence of bulk retained austenite [3, 18, 40]. Generally, the acicular reversed austenite can be obtained during the quenching, tempering or recrystallization of martensite [40]. Therefore, there are two categories of austenite contained in the tempered 431 and 431-2.5Cu MSS, including retained austenite and reversed austenite. Compared with the tempered Cu-free 431 MSS, the volume fraction of austenite in the tempered 431-2.5Cu MSS (i.e., 18.16%) was approximately doubled due to the addition of austenite stabilizer Cu. This is well consistent with Ye et al. [18], who reported that the volume fraction of austenite in the cast 15%Cr super MSS was increased with the increase of Cu content after tempering at 600 °C, with up to 39.55% at the Cu level of 3 wt%. Herein, the increased austenite in tempered 431-2.5Cu MSS could be ascribed to a synergistic effect between Ni and Cu [23, 24]. That is, the segregation of Cu at the grain boundary would reduce the stacking fault energy and accelerate the diffusion of Ni, which can provide the nucleation energy for reversed austenite in MSS [23, 24]. Meanwhile, the element of Ni can also enhance the enrichment of Cu and further promote the formation of reversed austenite [18, 23].

As seen from Fig. 8c and g, there are nano-sized precipitates distributed in the martensite matrix dispersively. In the tempered Cu-free 431 MSS, a small amount of particles with an average size of about 19 nm and width of 1.1 nm, which has been demonstrated as $Cr_{23}C_6$ by the SAED pattern. In marked contrast, the volume fraction of nano-precipitates was significantly enhanced in the tempered 431-2.5Cu MSS. The co-existence of ε-Cu and $Cr_{23}C_6$ has been confirmed by the SAED pattern, as indicated in Fig. 8h. Meanwhile, the particle 1 and 2 (Fig. 8g), can be easily distinguished by the EDS analysis, which could be identified as carbide (Fig. 8g1) and ε-Cu (Fig. 8g2), respectively.

Herein, the precipitation of ε-Cu nano-particles could be obtained during two processes. (1) Deposition process. As well-known, the time–temperature profile produced by LDED is quite different from that produced by conventional manufacturing technology [3]. During the LDED process, the material will experience unique thermal histories, including cyclic rapid heating and rapid cooling. As soon as the deposited material cools down from the liquid state, it will experience cyclic reheating during depositing adjacent tracks and subsequent layers [41]. This can induce many short temperature spikes, leading to an intrinsic heat treatment that can trigger clustering or nucleation of hardening precipitates during the LDED process without additional post heat treatment [42]. Also, Li et al. [43] demonstrated the presence of ε-Cu in the as-built samples prepared by LPBF technology.

(2) Tempering process. Generally, the crystal structure of nanoscale Cu particles undergoes a multi-stage transformation during the tempering process of MSS as follows: BCC-Cu → 9R-Cu → FCC-Cu [17, 24, 44]. Among them, the formation of coherent BCC-Cu could be attributed to the accumulation of Cu atoms in the Fe matrix during tempering, and thus improve the strength and ductility by coherent strengthening [17]. The displacive atomic motion of BCC-Cu could result in the formation of 9R-Cu particles due to the strain energy produced by the Cu enrichment [17]. In general, 9R-Cu particles can be categorized into two types, i.e., one is coherent and the other is incoherent. The mechanical properties are improved by coherent strengthening and Orowan bypassing mechanisms, respectively [45]. It has been established that the crystal structure of Cu precipitates is strongly dependent on the particle size [17, 46]. The critical diameters for the crystal structures transition from BCC-Cu to 9R-Cu and from 9R-Cu to 3R-Cu/FCC-Cu were determined to be 5 and 16 nm, respectively [17, 46]. In this work, a massive Cu precipitates with the size of 4–10 nm could be obtained after tempering at 600ºC for 1 h. Thus, we can speculate that the crystal structures of the Cu precipitates in the tempered 431-2.5Cu MSS are probably the coexistence of coherent BCC-Cu and 9R-Cu. Similarly, Sun et al. [17] observed both BCC-Cu and 9R-Cu with sizes of 4–12 nm in the tempered low-carbon Cu-bearing steels.

In order to elucidate the formation sequence of the nano-precipitates including the Cu-rich ε-Cu and carbide $Cr_{23}C_6$, the diffusion coefficient of Cr ($D_{Cr-\alpha}$) and Cu ($D_{Cu-\alpha}$) in martensite are calculated using the following formulas [47, 48]:

$$D_{Cr-\alpha} = 8.52\exp(-59,900/RT)$$
$$D_{Cu-\alpha} = 300\exp(-284,000/RT)$$

where D is diffusion coefficient (cm^2/s), R is the Boltzmann constant, and T is diffusion temperature (K). At the tempering temperature of 600 °C, the calculated $D_{Cr-\alpha}$ value

Fig. 8 TEM analysis of the tempered 431 MSS (**a–d**) and 431-2.5Cu MSS (**e–h**): **a** Bright-field (BF) image of the martensite lath; **b** Dark-field (DF) image of the austenite; **c** DF image of carbide; **d** SAED pattern of the martensite, austenite and $Cr_{23}C_6$; **e** BF image of the martensite lath; **f** DF image of the reversed and retained austenite together with SAED pattern; **g** DF image of nano-precipitates; **h** SAED pattern of $Cr_{23}C_6$ and ε-Cu. EDS analysis of particles 1 and 2 denoted in **g**: **g1** particle 1; **g2** particle 2
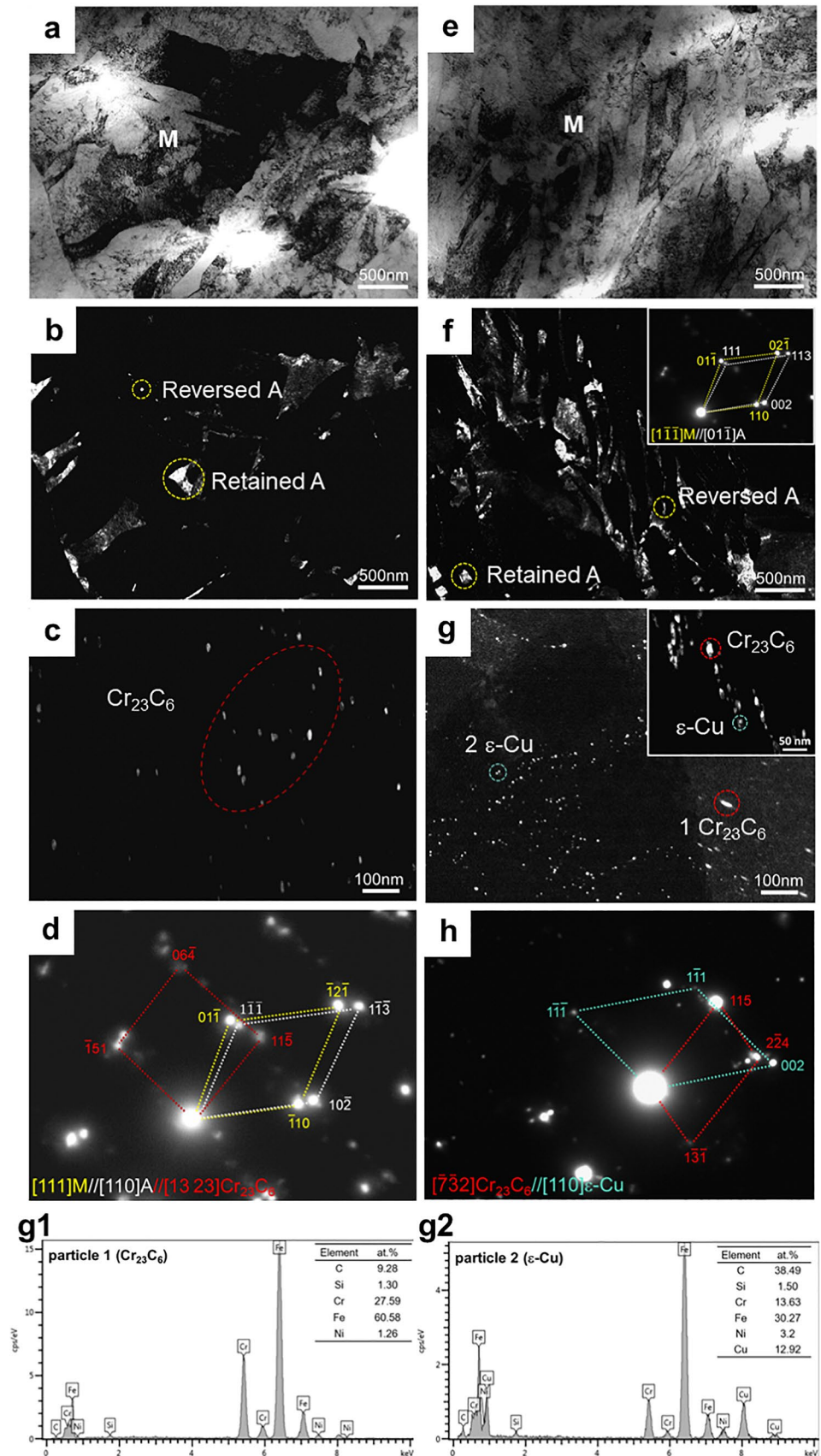
$(2.22 \times 10^{-3} \text{ cm}^2/\text{s})$ is twelve orders of magnitude higher than $D_{Cu-\alpha}$ $(3.07 \times 10^{-15} \text{ cm}^2/\text{s})$. This indicates that the $Cr_{23}C_6$ carbide is preferentially precipitated during tempering at 600 °C. In addition, Jung et al. [46] investigated the precipitation kinetics of Cu in martensite of a medium C steel, and found the carbide precipitation prior to the ε-Cu precipitation during tempering at 450–600 °C. Therefore, it can well explain the larger size of $Cr_{23}C_6$ particles compared to ε-Cu in Fig. 8g.

Based on the above results, the reasons accounting for the improvement in mechanical properties of the tempered 431-2.5Cu MSS could be closely related to the following three main microstructural factors.

(i) *Refined martensite laths*. The grain-refinement strengthening and toughing was generated owing to the refined martensite lathes, by the increased hindrance of dislocation motion and crack expansion. Therefore, both the strength and ductility of the tempered 431-2.5Cu MSS can be improved simultaneously.

(ii) *Enhanced austenite*. The existence of austenite (including retained austenite and reversed austenite) can induce the TRIP effect during the deformation, which provides a localized work-hardening effect and finally contributes to the improved ductility of MSS [24]. However, it is worth noting that the hardness and strength of reversed austenite are higher than the retained austenite owing to the much finer size of the former [49]. In this work, the larger volume fraction of fine reversed austenite can be obtained in the tempered 431-2.5Cu MSS due to the synergistic effect of Cu and Ni. The reversed austenite is a ductile phase, which can improve the ductility by absorbing the deformation work during plastic deformation in favor of the delayed necking [18, 50]. Meanwhile, the hardness and strength can be also maintained by the reversed austenite, owing to the improved stabilization of reversed austenite induced by the Cu element in martensite steel [48]. As revealed by Hu et al. [50], the reversed austenite with high stability is beneficial to the improvement of strength and toughness of the cast martensite steel after tempering at 620 °C for 1 h. This well explains the increased elongation without the sacrifice of strength for the tempered 431-2.5Cu MSS in comparison to the tempered 431 MSS.

(iii) *Precipitaed Cu-riched phase*. After tempering at 600 °C, the ε-Cu precipitates with the size of 5–10 nm are randomly dispersed in the matrix. The dispersively distributed ε-Cu nano-precipitates, having good coherency with the matrix of the tempered 431-2.5Cu MSS, could enhance the strength by increasing surface energy and coherent strain field in the dislocation shearing transformation [49]. Besides, the matrix can be significantly strengthened due to the dislocation multiplication and tangling after blocking the dislocation movement by the ε-Cu precipitates [17, 45]. In addition, Sun et al. [17] revealed that the precipitation of ε-Cu in the tempered 3.67 wt% Cu-bearing MSS could prevent the premature crack initiation and result in improved plasticity. Therefore, it can be reasonably believed that the ε-Cu precipitates is beneficial for both strength and ductility of the tempered 431-2.5Cu MSS.

4 Conclusions

In the present work, a high-strength and ductile Cu-bearing MSS with improved corrosion resistance were fabricated by the LDED technology and a single-step tempering treatment. The effects of Cu addition on the microstructure, mechanical properties and corrosion resistance of the tempered Cu-bearing (0–3.5 wt%) 431 MSS have been carefully investigated, and some interesting results have been obtained as demonstrated below:

(1) *Unique phase constitution* The tempered 431 MSS consists of lath martensite, austenite and nano-precipitates $Cr_{23}C_6$, while austenite and ε-Cu precipitates are promoted in the tempered Cu-bearing MSS. With the addition of Cu (0–3.5 wt%), the MSS samples exhibited a refined and more uniform microstructure than that of the Cu-free specimen.

(2) *Excellent properties* The element Cu could effectively improve the mechanical properties of the tempered 431 MSS by the synergistic effect of solution strengthening, grain-refinement strengthening and precipitation strengthening. The microhardness initially increased with increasing Cu content up to 2.5 wt% and then decreased. The tempered 431-2.5Cu specimen exhibits an excellent comprehensive properties, including a microhardness of 472 HV, UTS of 1576 MPa, YS of 1258 MPa, EL of 16.1%, together with a significantly enhanced corrosion resistance.

The current work has the potential to facilitate the laser manufacturing of high-strength and high-ductility steel components with superior mechanical properties and excellent corrosion resistance.

Appendix
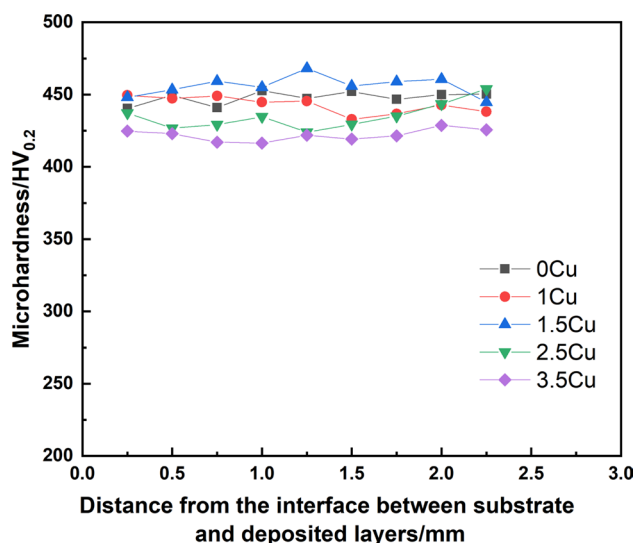
See Figs. 9, 10 and Table 3.

Fig. 9 The microhardness of the as-built AISI 431-xCu (x = 0, 1, 1.5, 2.5, 3.5). In as-built state, the microhardness of 0 Cu, 1Cu, 1.5Cu, 2.5Cu and 3.5Cu samples are 447 HV, 442 HV, 456 HV, 434 HV, and 421 HV, respectively. The date indicated that the addition of Cu has a little effect on the microhardness of the 431 MSS in as-built state
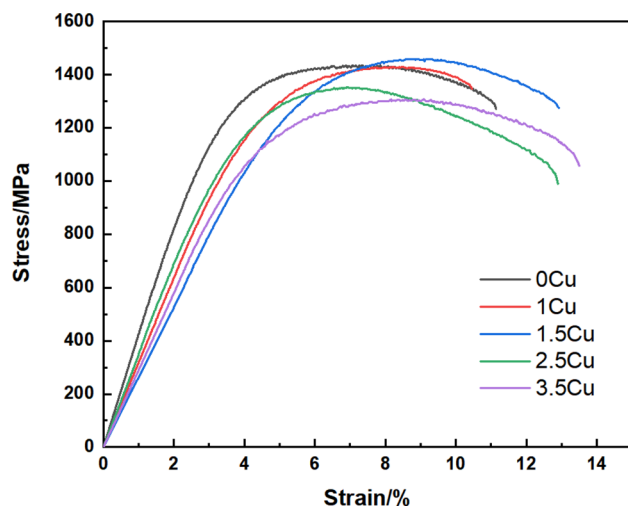

Fig. 10 Tensile curves of the as-built 431-xCu (x = 0, 1, 1.5, 2.5, 3.5). The date shows that the addition of can improve the ductile of the 431 MSS, without a significant beneficial effect on the strength enhancement

Table 3 The tensile results of the as-built 431 MSS with various Cu contents

Samples	UTS/MPa	YS/MPa	EL/%
0Cu	1427	1175	10.5
1Cu	1435	1183	10.1
1.5Cu	1462	1226	10.9
2.5Cu	1354	1164	12.6
3.5Cu	1269	1087	13.1

Declarations

References

1. Y. Liu, A. Li, X. Cheng, S.Q. Zhang, H.M. Wang, Effects of heat treatment on microstructure and tensile properties of laser melting deposited AISI 431 martensitic stainless steel. Mater. Sci. Eng. A **666**, 27–33 (2016). https://doi.org/10.1016/j.msea.2016.04.014

2. I. Hemmati, V. Ocelík, J.T.M. De Hosson, The effect of cladding speed on phase constitution and properties of AISI 431 stainless steel laser deposited coatings. Surf. Coat. Technol. **205**, 5235–5239 (2011). https://doi.org/10.1016/j.surfcoat.2011.05.035

3. B.C. Li, H.M. Zhu, C.J. Qiu, X.K. Gong, Laser cladding and in-situ nitriding of martensitic stainless steel coating with striking performance. Mater. Lett. **259**, 126829 (2020). https://doi.org/10.1016/j.matlet.2019.126829

4. H.M. Zhu, M.N. Ouyang, J.P. Hu, J.W. Zhang, C.J. Qiu, Design and development of TiC-reinforced 410 martensitic stainless steel coatings fabricated by laser cladding. Ceram. Int. **47**, 12505–12513 (2021). https://doi.org/10.1016/j.ceramint.2021.01.108

5. B. Aydogan, A. O'Neil, H. Sahasrabudhe, Microstructural and mechanical characterization of stainless steel 420 and Inconel 718 multi-material structures fabricated using laser directed energy deposition. J. Manuf. Process. **68**, 1224–1235 (2021). https://doi.org/10.1016/j.jmapro.2021.06.031

6. B.C. Li, H.M. Zhu, C.J. Qiu, D.K. Zhang, Development of high strength and ductile martensitic stainless steel coatings with Nb addition fabricated by laser cladding. J. Alloys Compd. **832**, 154985 (2020). https://doi.org/10.1016/j.jallcom.2020.154985

7. J.P. Hu, H.M. Zhu, J.W. Zhang, M.N. Ouyang, C.J. Qiu, J.A. Duan, Effects of TiC addition on microstructure, microhardness and wear resistance of 18Ni300 maraging steel by direct laser deposition. J. Mater. Process. Technol. **296**, 117213 (2021). https://doi.org/10.1016/j.jmatprotec.2021.117213

8. H.M. Zhu, J.W. Zhang, J.P. Hu, M.N. Ouyang, C.J. Qiu, Effects of aging time on the microstructure and mechanical properties of laser-cladded 18Ni300 maraging steel. J. Mater. Sci. **56**, 8835–8847 (2021). https://doi.org/10.1007/s10853-021-05841-1

9. L.D.V. Natália, A.C. Fernandes, R.A. Santos, T.F.A. Santos, S.L.U. Filho, Effect of laser parameters on the characteristics of a laser clad AISI 431 stainless steel coating on carbon steel substrate. JOM **73**, 2868–2877 (2021). https://doi.org/10.1007/s11837-021-04835-3

10. E.W.A. Figueredo, L.H.R. Apolinario, M.V. Santos, A.C.S. Silva, J.A. Avila, M.S.F. Lima, T.F.A. Santos, Influence of laser beam power and scanning speed on the macrostructural characteristics of AISI 316L and AISI 431 stainless steel depositions produced by laser cladding process. J. Mater. Eng. Perform. **30**, 3298–3312 (2021). https://doi.org/10.1007/s11665-021-05676-6

11. L.Q. Li, F.M. Shen, Y.D. Zhou, W. Tao, Comparative study of stainless steel AISI 431 coatings prepared by extreme-high-speed and conventional laser cladding. J. Laser Appl. **31**, 042009 (2019). https://doi.org/10.2351/1.5094378

12. K.P. Balan, A. Venugopal Reddy, D.S. Sarma, Effect of single and double austenitization treatments on the microstructure and mechanical properties of 16Cr–2Ni steel. J. Mater. Eng. Perform. **8**, 385–393 (1999). https://doi.org/10.1361/105994999770346963

13. A. Rajasekhar, G. Madhusudhan Reddy, T. Mohandas, V.S.R. Murti, Influence of austenitizing temperature on microstructure and mechanical properties of AISI 431 martensitic stainless steel electron beam welds. Mater. Des. **30**, 1612–1624 (2009). https://doi.org/10.1016/j.matdes.2008.07.042

14. K. Wang, B.H. Chang, J.S. Chen, H.G. Fu, Y.H. Lin, Y.P. Lei, K. Wang, B. Chang, J. Chen et al., Effect of molybdenum on the microstructures and properties of stainless steel coatings by laser cladding. Appl. Sci. **7**, 1065 (2017). https://doi.org/10.3390/app7101065

15. X.Y. Gao, H.Y. Wang, C. Ma, M. Lv, G. Sha, Y.M. Li, H.P. Ren, Micromechanism involved in ultrafine grained ferrite/martensite dual phase steels strengthened by nanoscale Cu-rich precipitates. Mater. Sci. Eng. A **819**, 141522–141525 (2021). https://doi.org/10.1016/j.msea.2021.141522

16. J. Wang, C.G. Li, X.J. Di, Effect of Cu content on microstructure and mechanical properties for high-strength deposited metals strengthened by nano-precipitation. Metals **12**, 1360 (2022). https://doi.org/10.3390/met12081360

17. H.L. Sun, D.D. Li, Y.P. Diao, Y. He, L.C. Yan, X.L. Pang, K.W. Gao, Nanoscale Cu particle evolution and its impact on the mechanical properties and strengthening mechanism in precipitation-hardening stainless steel. Mater. Charact. **188**, 111885 (2022). https://doi.org/10.1016/j.matchar.2022.111885

18. D. Ye, J. Li, W. Jiang, J. Su, K.Y. Zhao, Effect of Cu addition on microstructure and mechanical properties of 15% Cr super martensitic stainless steel. Mater. Des. **41**, 16–22 (2012). https://doi.org/10.1016/j.matdes.2012.04.036

19. Y.L. Huang, J.L. Zhao, J.R. Zhang, C.G. Yang, Y. Zhao, K. Yang, Y. Huang, J. Zhao, J. Zhang et al., Optimized antibacterial treatment for the Cu-bearing 420 stainless steel. Mater. Technol. **33**, 699–708 (2018). https://doi.org/10.1080/10667857.2018.1497574

20. L. Wang, C.F. Dong, C. Man, D.C. Kong, K. Xiao, X.G. Li, Enhancing the corrosion resistance of selective laser melted 15–5PH martensite stainless steel via heat treatment. Corros. Sci. **166**, 108427 (2020). https://doi.org/10.1016/j.corsci.2019.108427

21. J. Ma, Y.Y. Song, H.C. Jiang, L.J. Rong, Effect of Cu on the microstructure and mechanical properties of a low-carbon martensitic stainless steel. Materials **15**, 8849 (2022). https://doi.org/10.1016/j.corsci.2019.108427

22. C. Zhang, K.T. Yamanaka, H.K. Bian, A. Chiba, Corrosion-resistant carbide-reinforced martensitic steel by Cu modification. NPJ. Mat. Degrad. **3**, 30 (2019). https://doi.org/10.1038/s41529-019-0092-3

23. D. Ye, L.H. Yu, W. Jiang, K.Y. Zhao, J. Su, Synergistic effect of Cu and Ni on the formation of reversed austenite in super martensitic stainless steel. Ironmak. Steelmak. (2018). https://doi.org/10.1080/03019233.2018.1522099

24. M.C. Niu, K. Yang, J.H. Luan, W. Wang, Cu-assisted austenite reversion and enhanced TRIP effect in maraging stainless steels. J. Mater. Sci. Technol. **104**, 52–58 (2022). https://doi.org/10.1016/j.jmst.2021.06.055

25. Y. Liu, J.J. Yang, H. Yang, K.M. Li, Y.T. Qiu, W.C. Zhang, S.F. Zhou, Cu-bearing 316L stainless steel coatings produced by laser melting deposition: microstructure and corrosion behavior in simulated body fluids. Surf. Coat. Technol. **428**, 127868 (2021). https://doi.org/10.1016/j.surfcoat.2021.127868

26. W.F. Hu, H.N. Zhu, J.M. Hu, B.M. Li, C.J. Qiu, Influence of vanadium microalloying on microstructure and property of laser-cladded martensitic stainless steel coating. Materials **13**, 826 (2020). https://doi.org/10.3390/ma13040826

27. S. Takaki, M. Fujioka, S. Aihara, Y. Nagataki, T. Yamashita, N. Sano, Y. Adachi, M. Nomura, H. Yaguchi, Effect of copper on tensile properties and grain-refinement of steel and its relation to precipitation behavior. Mater. Trans. **45**, 2239–2244 (2004). https://doi.org/10.2320/matertrans.45.2239

28. Z.B. Jiao, J.H. Luan, M.K. Miller, C.T. Liu, Precipitation mechanism and mechanical properties of an ultra-high strength steel hardened by nanoscale NiAl and Cu particles. Acta Mater. **97**, 58–67 (2015). https://doi.org/10.1016/j.actamat.2015.06.063

29. A. Das, S.K. Das, S. Tarafder, Correlation of fractographic features with mechanical properties in systematically varied microstructures of Cu-strengthened high-strength low-alloy steel. Metall. Mater. Trans. A **40**, 3138–3146 (2009). https://doi.org/10.1007/s11661-009-9999-6

30. Y. Dai, S. Wang, Q.Y. He, C. Liu, X.Y. Wang, X. Li, L. Li, Y.J. Liu, C. He, Q.Y. Wang, Effect of microstructure on slip-induced crack initiation and early propagation of martensitic steel during high cycle fatigue. Int. J. Fatigue **167**, 107275 (2023). https://doi.org/10.1016/j.ijfatigue.2022.107275

31. G. Krauss, Martensite in steel: strength and structure. Mater. Sci. Eng. A **273**, 40–57 (1999). https://doi.org/10.1016/S0921-5093(99)00288-9

32. Y.Y. Song, D.H. Ping, F.X. Yin, X.Y. Li, Y.Y. Li, Microstructural evolution and low temperature impact toughness of a Fe–13%Cr–4%Ni–Mo martensitic stainless steel. Mater. Sci. Eng. A **527**, 614–618 (2010). https://doi.org/10.1016/j.msea.2009.08.022

33. H. Kong, Z. Jiao, J. Lu, C.T. Liu, Low-carbon advanced nanostructured steels: microstructure, mechanical properties, and applications. Sci. China Mater. **64**, 1580–1597 (2021). https://doi.org/10.1007/s40843-020-1595-2

34. R.L. Xiong, H.B. Peng, T.W. Zhang, J.W. Bae, H.S. Kim, Y.H. Wen, Superior strain-hardening by deformation-induced nano-HCP martensite in Fe–Mn–Si–C high- manganese steel. Mater. Sci. Eng. A **824**, 141864 (2021). https://doi.org/10.1016/j.msea.2021.141864

35. M.H. Zhang, L.H. Sun, Y.L. Liu, Y.L. Feng, N. Xu, H.Y. Chen, Y.D. Wang, In-situ investigation of strengthening and strain hardening mechanisms of Cu-added medium-Mn steels by synchrotron-based high-energy X-ray diffraction. J. Mater. Res. Technol. **24**, 2952–2964 (2023). https://doi.org/10.1016/j.jmrt.2023.03.209

36. L. Qi, A.G. Khachaturyan, J.W. Morris, The microstructure of dislocated martensitic steel: theory. Acta Mater. **76**, 23–39 (2014). https://doi.org/10.1016/j.actamat.2014.04.038

37. G. Miyamoto, N. Iwata, N. Takayama, T. Furuhara, Mapping the parent austenite orientation reconstructed from the orientation of martensite by EBSD and its application to ausformed martensite. Acta Mater. **58**, 6393–6403 (2010). https://doi.org/10.1016/j.actamat.2010.08.001

38. B. Xiao, L.Y. Xu, C. Cayron, J. Xue, G. Sha, R. Logé, Solute-dislocation interactions and creep-enhanced Cu precipitation in a novel ferritic-martensitic steel. Acta Mater. **195**, 199–208 (2020). https://doi.org/10.1016/j.actamat.2020.05.054

39. J. Hidalgo, M.J. Santofimia, Effect of prior austenite grain size refinement by thermal cycling on the microstructural features of as-quenched lath martensite. Metall. Mater. Trans. A **47**, 5288–5301 (2016). https://doi.org/10.1007/s11661-016-3525-4

40. Y.P. Zhang, D.P. Zhan, X.W. Qi, Z.H. Jiang, Austenite and precipitation in secondary-hardening ultra-high-strength stainless steel. Mater. Charact. **144**, 393–399 (2018). https://doi.org/10.1016/j.matchar.2018.07.038

41. P. Kürnsteiner, M.B. Wilms, A. Weisheit, P. Barriobero-Vila, E.A. Jägle, D. Raabe, Massive nanoprecipitation in an Fe–19Ni–xAl maraging steel triggered by the intrinsic heat treatment during laser metal deposition. Acta Mater. **129**, 52–60 (2017). https://doi.org/10.1016/j.actamat.2017.02.069

42. P. Kürnsteiner, M.B. Wilms, A. Weisheit, B. Gault, E.A. Jägle, D. Raabe, High-strength Damascus steel by additive manufacturing. Nature **582**, 515–519 (2020). https://doi.org/10.1038/s41586-020-2409-3

43. K. Li, J.B. Zhan, T.B. Yang, A.C.S. Tan, Q. Tang, H.J. Cao, L.E. Murr, Homogenization timing effect on microstructure and precipitation strengthening of 17–4PH stainless steel fabricated by laser powder bed fusion. Addit. Manuf. **52**, 102672 (2022). https://doi.org/10.1016/j.addma.2022.102672

44. Y.U. Heo, Y.K. Kim, J.S. Kim, J.K. Kim, Phase transformation of Cu precipitates from bcc to fcc in Fe–3Si–2Cu alloy. Acta Mater. **61**, 519–528 (2013). https://doi.org/10.1016/j.actamat.2012.09.068

45. C. Zhang, M. Enomoto, T. Yamashita, N. Sano, Cu precipitation in a prestrained Fe-1.5 wt pct Cu alloy during isothermal aging. Metall. Mater. Trans. A **35**, 1263–1272 (2004). https://doi.org/10.1007/s11661-004-0300-8

46. J. Jung, M.S. Jung, S.M. Lee, E. Shin, H.C. Shin, Y.K. Lee, Cu precipitation kinetics during martensite tempering in a medium C steel. J. Alloys Compd. **553**, 299–307 (2013). https://doi.org/10.1016/j.jallcom.2012.11.108

47. A.W. Bowen, G.M. Leak, Solute diffusion in alpha-and gamma-iron. Metall. Trans. **1**, 1695–1700 (1970). https://doi.org/10.1007/BF02642019

48. W. Jiang, K. Zhao, Effect of Cu on the formation of reversed austenite in super martensitic stainless steel. Materials **16**, 1302 (2023). https://doi.org/10.3390/ma16031302

49. Y.H. Kim, J.H. Kim, T.H. Hwang, J.Y. Lee, C.Y. Kang, Effect of austenite on mechanical properties in high manganese austenitic stainless steel with two phase of martensite and austenite. Met. Mater. Int. **21**, 485–489 (2015). https://doi.org/10.1007/s12540-015-4480-0

50. J. Hu, L.X. Du, W. Xu, J.H. Zhai, Y. Dong, Y.J. Liu, R.D.K. Misra, Ensuring combination of strength, ductility and toughness in medium-manganese steel through optimization of nano-scale metastable austenite. Mater. Charact. **136**, 20–28 (2018). https://doi.org/10.1016/j.matchar.2017.11.058